

## "Origin of the extended Mars radar blackout of September 2017"

Beatriz Sánchez-Cano<sup>1</sup>, Pierre-Louis Blelly<sup>2</sup>, Mark Lester<sup>1</sup>, Olivier Witasse<sup>3</sup>, Marco Cartacci<sup>4</sup>, Roberto Orosei<sup>5</sup>, Hermann Opgenoorth<sup>6,1</sup>, Robert Lillis<sup>7</sup>, François Leblanc<sup>8</sup>, Stephen E. Milan<sup>1</sup>, Philip Conroy<sup>3</sup>, Nicolas Floury<sup>3</sup>, John M.C. Plane<sup>9</sup>, Andrea Cicchetti<sup>4</sup>, Raffaella Noschese<sup>4</sup>, Andrew J. Kopf<sup>10</sup>

<sup>1</sup> Radio and Space Plasma Physics Group, Department of Physics and Astronomy, University of Leicester, University Road, Leicester, LE1 7RH, UK.

<sup>2</sup> Institut de Recherche en Astrophysique et Planétologie (IRAP), Toulouse, France.

<sup>3</sup> European Space Agency, ESTEC, Keplerlaan 1, Noordwijk 2200 AG, The Netherlands.

<sup>4</sup> Istituto Nazionale di Astrofisica (INAF), Istituto di Astrofisica e Planetologia Spaziali (IAPS), Rome, Italy.

<sup>5</sup> Istituto di Radioastronomia (IRA), Istituto Nazionale di Astrofisica (INAF), Bologna, Italy

<sup>6</sup> Department of Physics, Umeå University, Linnaeus väg 24, 901 87 Umea, Sweden

<sup>7</sup> Space Sciences Laboratory, University of California, Berkeley, CA, USA

<sup>8</sup> LATMOS/CNRS, Sorbonne Université, UVSQ, CNRS, Paris, France

<sup>9</sup> School of Chemistry, University of Leeds, Leeds, UK

<sup>10</sup> Department of Physics and Astronomy, University of Iowa, Iowa City, IA, USA

**Corresponding author:** Beatriz Sánchez-Cano (bscmdr1@leicester.ac.uk)

### Key Points:

- A large space weather event caused negatively impacted radar performance for 10 days.
- Solar electron precipitation created a low ionospheric layer at ~90km on the nightside.
- The nightside ionization is comparable to dayside values.

**Key Words:** Mars' ionosphere, radar blackout, electron precipitation, space weather, solar energetic particles

1 **Abstract**

2 The Mars Advanced Radar for Subsurface and Ionosphere Sounding (MARSIS) on board Mars  
3 Express, which operates between 0.1 and 5.5 MHz, suffered from a complete blackout for 10 days  
4 in September 2017 when observing on the nightside (a rare occurrence). Moreover, the Shallow  
5 Radar (SHARAD) onboard the Mars Reconnaissance Orbiter, which operates at 20 MHz, also  
6 suffered a blackout for 3 days when operating on both day and nightsides. We propose that these  
7 blackouts are caused by solar energetic particles (SEP) of few tens of keV and above associated  
8 with an extreme space weather event between 10 and 22 September 2017, as recorded by the  
9 MAVEN mission. Numerical simulations of energetic electron precipitation predict that a lower  
10  $O_2^+$  nighttime ionospheric layer of magnitude  $\sim 10^{10} \text{ m}^{-3}$  peaking at  $\sim 90 \text{ km}$  altitude is produced.  
11 Consequently, such a layer would absorb radar signals at HF frequencies and explain the  
12 blackouts. The peak absorption level is found to be at 70km altitude.

13

14 **Plain Language Summary**

15 Several instrument operations, as well as communication systems with rovers at the surface,  
16 depend on radio signals that propagate throughout the atmosphere of Mars. This is the case also  
17 for two radars that are currently working in Mars' orbit, sounding the ionosphere, surface and  
18 subsurface of the planet. In mid-September 2017, a powerful solar storm hit Mars, producing a  
19 large amount of energetic particle precipitation over a 10 day period. We have found that high  
20 energy electrons ionized the atmosphere of Mars, creating a dense layer of ions and electrons at  
21  $\sim 90 \text{ km}$  on the Martian nightside. This layer attenuated radar signals continuously for 10 days,  
22 stopping the radars to receive any signal from the planetary surface. In this work, we assess the  
23 properties of this layer in order to understand the implications of this kind of phenomenon for  
24 radar performance and communications.

25

26

27

28

29

## 30 **1. Introduction**

31 Precipitation of energetic charged particles as well as ablation of interplanetary dust particles can  
32 produce a prompt rise in the electron density of the ionosphere of Mars below 100 km, where the  
33 plasma density is typically very low (e.g. Lillis et al., 2018; Espley et al., 2007; Pesnell and  
34 Grebowsky, 2000; Molina-Cuberos et al., 2003). At these altitudes, the electron-neutral collision  
35 frequency is of the same order as the high-frequency (HF) frequency of the radars. Therefore, if  
36 electrons are present, radio waves at these frequencies can be attenuated, or in the worst case,  
37 totally absorbed. Consequently, a severe degradation of performance of radio-based instruments  
38 such as radars and sounders, as well as navigation and communication systems can occur (e.g.  
39 Withers, 2011). Previous research has shown that radio blackouts at Mars may occur more often  
40 than expected (e.g. Espley et al., 2007) and with long-lasting effects, especially after strong space  
41 weather activity. Therefore, a good understanding of this phenomenon is needed on the eve of  
42 the era of the human exploration of Mars.

43 It is known that solar energetic particles (SEPs) (e.g. Espley et al., 2007; Němec et al., 2014),  
44 corotating interaction regions (CIRs) (e.g. Morgan et al., 2010), interplanetary coronal mass  
45 ejections (ICMEs) (e.g. Campbell et al., 2014; Morgan et al., 2014; Andrews et al., 2016), meteoric  
46 showers (e.g. Pesnell and Grebowsky, 2000; Witasse et al., 2001; Molina-Cuberos et al., 2003),  
47 and areas over closed crustal magnetic field lines (e.g. Němec et al., 2015) can cause some radar  
48 disruptions. All these scenarios are believed to produce a rise in the electron density of the lower  
49 ionosphere below 100 km, where even a small amount of extra ionization significantly increases  
50 the signal attenuation (e.g. Nielsen et al., 2007). Some work suggests that solar protons of tens of  
51 MeV could be the cause for these absorption layers, similar to the polar cap absorption (PCA)  
52 events at Earth (e.g. Morgan et al., 2006; Sheel et al., 2012). However, electron precipitation is  
53 considered to be the dominant source of ionization in Mars' nightside upper atmosphere (e.g. Fox  
54 et al., 1993; Leblanc et al., 2006; Fillingim et al., 2007; Lillis et al., 2011; 2018; Lillis and Fang,  
55 2015), together with plasma transport.

56 On September 2017, after one of the strongest space weather energetic particle event of the latest  
57 fifteen years hit Mars, the Mars Advanced Radar for Subsurface and Ionosphere Sounding  
58 (MARSIS) on board Mars Express (MEX) and the Shallow Radar (SHARAD) onboard the Mars  
59 Reconnaissance Orbiter (MRO) suffered long-lasting signal blackouts for several days. It appears  
60 that this blackout event was caused by a global absorption layer, including the deep-nightside  
61 region (total darkness). The locations of the blackouts are shown in Figure 1 and in the  
62 Supporting Information (SI) file. Its long duration is itself remarkable, as it suggests that a near  
63 permanent lower ionospheric layer globally stopped HF communications with the surface for

64 several days. Moreover, the fact that the layer was also formed on the deep-nightside is of great  
65 interest, as radars typically work better in that region because the critical plasma frequency of  
66 the ionosphere (as determined by the peak electron density) is typically well below the radar  
67 carrier frequency (e.g. Safaeinili et al., 2003; 2007; Mougnot et al., 2008; Cartacci et al., 2013;  
68 2018; Sánchez-Cano et al., 2015a), i.e. the ionosphere is very tenuous (Girazian et al., 2017a;  
69 2017b).

76 The objective of this work is to assess the properties of such a putative lower ionospheric layer  
77 that was created on the deep-nightside during September 2017. The main aim is to understand  
78 which ionizing agent can create such layers, as well as the electron densities required at different  
79 altitudes to inhibit the radar link to the ground.

80

## 81 **2. Space Weather Context**

82 Figures 2a-c display Mars Atmosphere and Volatile Evolution (MAVEN) mission observations as  
83 a function of time for the period 4-29 September 2017. The irradiance data is taken from the  
84 Extreme-Ultraviolet (EUV) monitor in the wavelengths 0.1–7nm (Eparvier et al., 2015), and the  
85 ion and electron differential flux spectra are from the Solar Energetic Particle instrument  
86 (hereinafter MAVEN-SEP) (Larson et al., 2015). Only data from the MAVEN-SEP1 sensor's  
87 forward look direction has been plotted although we note that both forward and rear look  
88 directions show similar observations.

89 The Active Region (AR) 12673 at the western limb of the solar disk during September 2017 was  
90 very productive in terms of Earth-directed X-class solar flares and ICMEs (e.g. Redmon et al., 2018;  
91 Jiggins et al., 2018). The same AR also emitted a X8.2-class flare on 10 September 2017 starting  
92 at ~15:35 UT and peaking at ~16:06 UT, and released a powerful CME at ~15:54 UT (Guo et al.,  
93 2018; Lee et al., 2018). At Mars, 160° from Earth in the ecliptic plane, the peak of the flare was  
94 observed at 16:11 (~5 min after Earth) (Figure 2a). SEP electrons (20-200 keV) started to arrive  
95 at Mars at ~19:20 UT (~3h later, Figure 2c), and ions (20 keV-6 MeV) at ~22:00 UT (~6h later,  
96 Figure 2b). Lee et al. (2018) showed that 15-220 MeV SEP protons also penetrated the MAVEN-  
97 SEP instrument from ~22:00 UT, although direct energy flux measurements are not available as  
98 the instrument is optimized to measure 20 keV-6 MeV protons. Both SEP electrons and ions  
99 (Figures 2b-c) show a sharp flux increase on 12 September 2017 (reddish colors) when the ICME  
100 shock passed over Mars. After that, SEP electrons gradually decreased over 13 days until 23  
101 September, but with a small enhancement on 18 September caused by another solar flare (Figures  
102 2a and 2c). In contrast, SEP ions sharply decreased on 14 September when the ICME completed

103 its passage past Mars. After that, the ion flux was very low until 20 September, when there was a  
104 further notable rise (reddish colors) most probably caused by the passage of the flank of another  
105 ICME magnetically well-connected to Mars (see ENLIL run at  
106 [https://ccmc.gsfc.nasa.gov/database\\_SH/Leila\\_Mays\\_120817\\_SH\\_9.php](https://ccmc.gsfc.nasa.gov/database_SH/Leila_Mays_120817_SH_9.php), Lee et al., 2018).

107

### 108 **3. Radar Attenuation**

#### 109 **3.1 MARSIS and SHARAD Observations**

110 The MARSIS radar on board Mars Express (Chicarro et al., 2004) is a nadir-looking pulse-limited  
111 radar sounder with a 40-m dipole antenna. The radar has two different operational modes (e.g.  
112 Picardi et al., 2004; Orosei et al., 2016): (1) A Sub-Surface mode designed to sound the surface  
113 and subsurface of the planet with frequencies centered at 1.8, 3, 4, and 5 MHz. Two different  
114 frequencies are transmitted in sequence with a small delay (450  $\mu$ s) between them to avoid the  
115 possibility of overlapping during the receiving phase. The selection of the transmitted frequencies  
116 mainly depends on the solar zenith angle (SZA) conditions at the time of the observations. Both  
117 transmitted bandwidths are always chosen to be well above the critical plasma frequency of the  
118 ionosphere below, in order to be able to propagate with the smallest possible degradation. For  
119 this study, 3 and 4 MHz were the operational MARSIS frequencies since the observations were  
120 planned to be collected during the nightside. (2) An Active Ionospheric Sounding (AIS) mode  
121 designed to sound the topside ionosphere from the spacecraft location up to the critical plasma  
122 frequency of the ionosphere with a sweep of frequencies between 0.1 and 5.5 MHz. In AIS-mode,  
123 the radar frequencies can also be reflected from the Martian surface if the carrier frequency is  
124 larger than the critical plasma frequency, and the total electron content of the bottomside  
125 ionosphere is thin enough not to attenuate the signals. Complementary to MARSIS, the SHARAD  
126 radar onboard Mars Reconnaissance Orbiter (Zurek and Smrekar, 2007) also sounds the Martian  
127 surface-subsurface with a linear chirp signal centered at 20 MHz and a bandwidth of 10 MHz (Seu  
128 et al., 2004), which is always higher than the critical plasma frequency.

129 Figures 3a-b show several radargrams from MARSIS and SHARAD. A radargram is a 2-D  
130 backscattered power image of the surface-subsurface reflections built from the radar  
131 measurements along the orbit. Time delay is typically plotted on the vertical axis and the along-  
132 track distance on the horizontal axis. The brightness of the pixel is a function of the strength of  
133 the echo measured in decibels (dB). During September 2017, MARSIS was sampling the southern  
134 hemisphere of Mars on the deep-nightside, although not on every MEX orbit. SHARAD in contrast  
135 was sampling both dayside and nightside, and both hemispheres due to MRO's sun-synchronous

136 low 250x320 km orbit. Different symbols in Figure 2d show the timing when MARSIS and  
137 SHARAD were in operation. Empty symbols indicates when both radars observed a reflection  
138 from the surface, and filled symbols when the surface reflection was not received (i.e. the radars  
139 were transmitting but not receiving signals). In addition, a green diamond indicates when the  
140 surface reflection was highly blurry for the SHARAD radar. While the blackout lasted at least ~10  
141 days for both MARSIS operational modes, the blackout lasted only ~3 days for SHARAD because  
142 radio absorption processes are frequency-dependent (see Section 4). Figure 2 clearly  
143 demonstrates that SEP electrons were present during the entire period of the radar blackout and  
144 therefore suggests that precipitating electrons, rather than ions, were responsible for the creation  
145 of a lower nightside ionospheric layer that absorbed the radar signals (see the discussion section  
146 for details).

### 147 **3.2. Estimation of the Attenuation**

148 To estimate the MARSIS radar attenuation during this event, we have compared the signal power  
149 versus delay time for orbit 17362 (one of those affected by the blackout) with previous orbits  
150 close in time when the radars operated at the same frequency, on the non-illuminated nightside  
151 ( $SZA > 130^\circ$ ), and over the same region of the planet. Orbit 17362 was chosen because the surface  
152 area tracked by MARSIS is sufficiently flat for a region of the southern hemisphere, in order to  
153 minimize the topography and composition effect on the signal power reflected back to the radar.  
154 Only radargrams from the nadir-pointing direction are used in this analysis. Peaks at  $1.7\text{-}1.9 \times 10^{-4}$   
155 s in Figure 4a correspond to the power signal reflection of the Martian surface in orbits not  
156 affected by the blackout. The average power signal of the surface reflection in this area is 60 dB  
157 for 4 MHz, and 59 dB for 3 MHz. During the space weather event (black profiles, Figure 4a), the  
158 MARSIS signal power fell to the background noise level that was on average  $24 \pm 9$  dB for 4 MHz  
159 and  $25 \pm 9$  dB for 3 MHz for the whole orbit. We define the noise uncertainty as 1.5 times the  
160 standard deviation of the noise in Figures 4a and 4b. The proposed noise threshold is a reasonable  
161 solution in order to identify with good accuracy the leading edge of the signal that is critical for  
162 correct estimations of the signal travel time. Therefore, after considering the difference between  
163 the nominal power signal and the noise level, the radar signals were attenuated by at least  $36 \pm 9$   
164 dB for 4 MHz and  $34 \pm 9$  dB for 3 MHz. Assuming that this attenuation operates in both directions  
165 (spacecraft-surface-spacecraft), the lower limit attenuation that we can estimate for one way is  
166 at least  $18 \pm 9$  and  $17 \pm 9$  dB for 4 and 3 MHz, respectively.

167 The same procedure was carried out for the SHARAD radar at 20 MHz. Previous orbits over the  
168 same flat region of orbit 52179 were compared (Figure 4b), obtaining a two-way attenuation of  
169  $19.0 \pm 3.3$  dB, and a one-way attenuation of  $9.5 \pm 3.3$  dB. We note that the sign of the MARSIS and

170 SHARAD power signals are different because both instruments have a different reference level.  
 171 This is not an issue for our study, as we are estimating the absolute value of the attenuation on  
 172 each radar separately.

173

#### 174 **4. Radio Attenuation Theory**

175 A radar signal (electromagnetic wave) crossing the Martian ionosphere can experience four  
 176 different effects (Safaenili et al., 2003; Campbell et al., 2014): (1) an increase in the time delay  
 177 with respect to that expected from the speed of light in vacuum, (2) distortion of the signal phase  
 178 due to the frequency dependence of the refractive index (radar signals close to the critical  
 179 frequency of the ionosphere), (3) attenuation of the signal amplitude that is controlled by thermal  
 180 electron collisions with the neutrals, and (4) Faraday rotation effects over strong crustal magnetic  
 181 field regions (this effect is minor compared to attenuation (Safaenili et al., 2003)). In this work,  
 182 radar signals are expected to be totally lost mainly due to attenuation processes since the  
 183 operational frequencies of both radars are much larger than the expected ionospheric critical  
 184 frequency of the normal ionosphere (see Section 5), while this new absorbing layer is expected  
 185 to be formed below 100 km where the neutral atmosphere is denser. Nevertheless, we note that  
 186 for those cases when the surface is highly blurry (Figure 4b), large signal phase delays must have  
 187 been as important as absorption processes.

188 Neglecting any effect of Mars' crustal magnetic fields, radio waves can be attenuated during their  
 189 propagation through the ionosphere as described by equation (1). We neglect the effect of the  
 190 crustal fields because their influence on radio-propagation can be considered weak (Nielsen et  
 191 al., 2007), and also, because the radio blackouts occurred everywhere over the planet and not  
 192 only over crustal field areas (see Figure 1 and SI). Combining equations (1) and (2), the  
 193 attenuation can be rewritten as (3).

194

$$A(h) = 8.686 \frac{2 \pi f}{c} \operatorname{Im} \left( \sqrt{1 - \frac{(2 \pi f_p)^2}{(2 \pi f)^2 - i 2 \pi \nu f}} \right) \quad (1)$$

$$f_p = 8.98 \sqrt{N_e(h)} \quad (2)$$

$$A(h) = 4.61 \cdot 10^7 N_e(h) \frac{\nu(h)}{(2 \pi f)^2 + \nu^2(h)} \quad (3)$$

195 where  $A$  is the attenuation in  $\text{dB}\cdot\text{m}^{-1}$ ,  $\text{Im}$  is the imaginary term,  $f$  and  $f_p$  are the carrier and plasma  
 196 frequencies respectively in Hz,  $c$  is the speed of light,  $\nu$  is the momentum-transfer electron-neutral  
 197 collision frequency in  $\text{s}^{-1}$ , and  $N_e$  is the electron density in  $\text{m}^{-3}$ .

198 In the lower ionosphere, the main neutral component is carbon dioxide ( $\text{CO}_2$ ), and therefore  $\nu$  can  
 199 be set equal to the electron- $\text{CO}_2$  collision frequency (Witasse et al., 2001). In this study, we use  
 200 the well-accepted  $\nu$  formula described by Schunk and Nagy (2009), using equation (4) which is  
 201 based on Itikawa (1978) who considers the electron temperature,  $T_e$ , and  $\text{CO}_2$  neutral density,  $n$ ,  
 202 as inputs.

$$\nu(e^- - \text{CO}_2) = 3.68 \cdot 10^{-8} n (1 + 4.1 \cdot 10^{-11} |4500 - T_e|^{2.93}) \quad (4)$$

203 Since  $\nu$  is directly proportional to  $n$ ,  $\nu$  increases with decreasing altitude and this results in a larger  
 204 radar absorption in the lower atmosphere. Consequently, even a very small ionospheric layer at  
 205 low altitude has a larger effect on the attenuation than the main dayside layer peaking at 130-140  
 206 km (Witasse et al., 2001).

207

## 208 5. Ionospheric Modelling

209 In order to assess the main properties of the lower ionospheric layer created during this event,  
 210 we use the Mars version of the numerical/physical IRAP plasmasphere-ionosphere model (IPIM)  
 211 (Marchaudon and Blelly, 2015). IPIM is based on the TRANSCAR and TRANSMARS codes (e.g.,  
 212 Blelly et al., 1996; 2005; Morel et al., 2004; Ramírez-Nicolás et al., 2016; Sánchez-Cano et al.,  
 213 2015b; 2018; Witasse, 2000; Witasse et al., 2002; 2003), in which transport equations for the  
 214 ionized species are based on a 16 moment approximation, and the suprathermal electron fluxes  
 215 are computed after solving their steady state transport equation. The model also takes into  
 216 account for primary and secondary collisions with the neutrals and excitation and ionization  
 217 processes, either by solar radiation illumination or electron impact (Blelly et al., 2019). The Mars  
 218 version uses the Mars Climate Database (MCD) (version 5.3) as input for neutral atmospheric  
 219 conditions (e.g., Forget et al., 1999; Millour et al., 2015), and it includes the six major ion species  
 220 ( $\text{O}_2^+$ ,  $\text{NO}^+$ ,  $\text{O}^+$ ,  $\text{CO}_2^+$ ,  $\text{N}_2^+$ , and  $\text{H}^+$ ) in the Martian ionosphere. Other ion species are not considered  
 221 in this study because their densities are several orders of magnitude smaller. The simulation was  
 222 performed for the prevailed conditions during the MARSIS observations (i.e. similar solar activity  
 223 level, solar zenith angle and planet location) on 10 September 2017, at 23:00:00 UT, at the  
 224 beginning of the Mars space weather event. Since Figure 2 strongly suggests that electrons were  
 225 responsible for this blackout, a flux of downward precipitating electrons at 500 km was included  
 226 in the model as a source of ionization (Figure 5a). This precipitating electron flux was fitted only

227 to the MAVEN-SEP observations for the higher energies (above 20 keV) as we are sure that these  
228 electrons are not originating from Martian environment. We did not considered MAVEN Solar  
229 Wind Electron Analyzer (SWEA) observations at low altitude because they were taken when  
230 MAVEN was on the dayside and there was a strong risk that we account for photoelectrons in the  
231 precipitation flux when this simulation is focused on the deep-nightside. The simulation  
232 considers different scattering angles with respect to the vertical, being positive for the downward  
233 direction and negative for the upward direction. Figure 5a also shows the electron flux at two  
234 different altitudes. At 500 km, most of the flux precipitates in the downward direction with almost  
235 no scattering due to upper boundary conditions for the flux and low atmospheric densities. At  
236 70km, the flux is isotropic due to scatter on a denser atmosphere. Only secondary electrons  
237 remain at lower energies ( $\sim 1-50$  eV). Though the input flux is mainly in the range  $\sim 10$ keV (based  
238 on MAVEN-SEP observations, Figure 5a), we clearly see a low energy contribution (below 500 eV)  
239 present at all altitudes resulting from secondary electrons created by collisions on neutrals. This  
240 is also observed when plotting the flux profile with altitude. Figure 5b shows the flux profile of  
241 four selected energies in Figure 5a. Large energies, such as 10 keV have a primary contribution  
242 to the atmosphere around  $\sim 90-100$  km. However, lower energies such as 500 eV, as said before,  
243 have two kind of contributions: a direct one above 100 km, and a secondary one caused by  
244 secondary electron production at  $\sim 60-70$  km.

245 Figure 6 shows the electron penetration depth as a function of energy. It was obtained by  
246 calculating the electron production rate associated with a mono-energetic beam of electron  
247 precipitation flux for energy in the range 50 eV -100 keV, and then assuming that the altitude for  
248 which the electron production rate reaches a maximum (white line) corresponds to the altitude  
249 where the precipitating electrons are stopped (Rees, 1989). For energies higher than 500 eV, the  
250 white line is split into two as particles are deposited at two different altitudes: the lower one  
251 corresponds to direct penetration of the very energetic population, while the upper one is caused  
252 by secondary electron production in the atmosphere. This figure indicates that electrons of  
253 energy 10 keV are able to penetrate at least down to 60km. By using a precipitation flux fitted on  
254 MAVEN-SEP data, we get the ion density profiles shown in Figure 5c. The simulation predicts that  
255 precipitation of energetic electrons created a layer mainly composed by  $O_2^+$ , and  $NO^+$  below  
256  $\sim 60$ km, with a maximum density of  $\sim 10^{10} m^{-3}$  at  $\sim 90$  km. The width of the layer corresponds to  
257 the split discussed in Figure 6. The altitude of this layer agrees well with previous observations  
258 of the nightside ionosphere using the radio science technique when solar energetic particle  
259 precipitation occurred, although not as intense as for this event. However, the magnitude of the  
260 simulation layer for this event is several orders of magnitude larger than the previous nightside  
261 observations (Withers et al., 2012) because of the larger precipitating fluxes. The density of this

262 simulated layer is comparable to densities of the dayside ionospheric secondary peak, which is  
263 typically found at 110 km (e.g. Sánchez-Cano et al., 2013; 2016).

264 The radar attenuation caused by this layer was then estimated using the simulation outputs.  
265 Figure 5e shows the  $\nu$  profile obtained from equation (4), and the modelled electron and neutral  
266 temperatures (cyan and red respectively) and CO<sub>2</sub> density (blue) in Figure 5d. The simulation  
267 solves the energy balance for thermal electrons and the electron temperature profile results  
268 mainly from the thermal equilibrium between cooling by neutrals and ions and heating by  
269 suprathermal electrons. The  $\nu$  profile is in very good agreement with previous estimates (e.g.  
270 Nielsen et al. 2007; Witasse et al., 2001). To a first approximation, Figure 5e also shows at which  
271 altitude range each radar frequency will suffer its largest attenuation (i.e. when  $f$  equals  $\nu$ ). For  
272 MARSIS (4MHz), the attenuation is more efficient at  $\sim 70$ km, while it is at  $\sim 58$  km for SHARAD  
273 (20MHz). Finally, Figure 5f shows the attenuation profiles with altitude for 3 different frequencies,  
274 based on equations (2), (3) and (4), and on Figures 5c, 5d and 5e. All of them peak at  $\sim 70$ km.  
275 Another way of showing these results is in the form of cumulative attenuation profiles, as in  
276 Figure 5g. The total attenuation for each  $f$  is obtained by integrating each attenuation profile in  
277 Figure 5f, giving 79, 50, and 4 dB attenuation for 3, 4 and 20 MHz respectively. Therefore, the  
278 attenuation caused by the lower ionospheric layer was large enough to cause the radar  
279 attenuation measured by MARSIS, and of the same order of the attenuation measured by SHARAD  
280 (Section 3.2).

281 In order to determine the minimum ionization which is able to produce a signal loss at a certain  
282 height, we have estimated how much the total attenuation varies with small changes in density  
283 and altitude. Figure 7 left panel shows the total attenuation behavior with frequency for a  $N_e$   
284 profile with the same peak density and shape as in Figure 5c but formed at different altitudes  
285 (color-coded). For reference, the measured MARSIS and SHARAD attenuations are also indicated.  
286 The total attenuation is larger for smaller frequencies as expected, and also, for lower peak  
287 altitudes. For MARSIS, the attenuation caused by a layer with magnitude  $\sim 10^{10}$  m<sup>-3</sup> and similar  
288 shape to Figure 5c at 100 km (or lower) would be sufficient to explain the radar blackout. For  
289 SHARAD, it would be sufficient if it were below 85 km. Figure 7 right panel shows the total  
290 attenuation behavior with frequency for a  $N_e$  profile with the same peak altitude and shape as in  
291 Figure 5c but formed with different peak densities (color-coded). As before, the total attenuation  
292 is larger for lower frequencies, and in this case, for higher peak densities. For MARSIS, the  
293 attenuation caused by a layer of magnitude  $3.5 \times 10^9$  m<sup>-3</sup> (or higher) at 90 km would be sufficient  
294 to explain the radar blackout. For SHARAD, it would be sufficient with  $4.2 \times 10^{11}$  m<sup>-3</sup>.

295

296 **6. Discussion**

297 It is generally accepted that during a SEP event, nightside electron densities are substantially  
298 enhanced and consequently, surface reflections from radar wave propagation tend to disappear  
299 (e.g. Espley et al., 2007; Němec et al., 2014). However, these absorbing ionospheric layers formed  
300 at low altitude have never been directly measured at Mars, making the estimates of their main  
301 characteristics difficult. One of the major difficulties is to understand the cause of the long-  
302 duration of these blackouts (several days) because the lifetime of the main ionospheric ion,  $O_2^+$ ,  
303 is of the order of a few minutes due to fast dissociative recombination with electrons (Bones et  
304 al., 2015). Therefore, the ionization source must be continuous in all these cases for a level of  
305 several days, which is rare for a space weather event. An alternative interpretation of these events  
306 is that the layer is composed of metallic ions such as  $Mg^+$  and  $Fe^+$ , as in sporadic layers in the  
307 terrestrial lower  $E$  region (Plane, 2003). These atomic ions have a relatively long lifetime against  
308 neutralization because radiative recombination with electrons is relatively slow, so they first  
309 need to form molecular ions (Plane et al., 2018).  $Mg^+$  ions have been continuously observed at  
310 Mars by the Imaging Ultraviolet Spectrograph (IUVS) instrument on MAVEN in a layer peaking  
311 around 90-95 km and with a typical concentration of  $4-8 \times 10^8 \text{ m}^{-3}$  (Crismani et al., 2017).  
312 Moreover, a recent model has shown that  $Mg^+$  should be the major form of magnesium above 80  
313 km (Figure 7 in Plane et al., 2018), and thus additional  $Mg^+$  would be unlikely to be produced by  
314 SEP from neutral Mg species, either directly or by charge transfer with  $O_2^+$ . In fact, the IUVS  
315 instrument did not observe a significant increase of  $Mg^+$  during September 2017 (M. Crismani,  
316 NASA Goddard Space Flight Center, pers. comm.). This corroborates that  $O_2^+$  and possibly  $NO^+$  are  
317 indeed the main ions that formed the layer.

318 In the case of space weather events, it is not clear whether the main sources of ionization are solar  
319 wind electrons or protons. Most of the previous studies suggested that energetic solar wind  
320 protons seem to be responsible (e.g. Morgan et al., 2006; Sheel et al., 2012; Němec et al., 2015).  
321 However, Ulusen et al. (2012) found that in 4 of the 6 events that they studied, an increase in  
322 electron density below 100 km occurred caused by electrons of 10–20 keV energy, which is  
323 consistent with the event in the present study. Considering that the ionization source must be  
324 continuous in order to explain the long life-time duration of the absorption  $O_2^+$  layer below 100  
325 km, Figure 2 shows that only the continuous enhanced SEP electron flux for  $\sim 10$  days is able to  
326 explain all the radar blackouts seen by both spacecraft because the SEP ion flux was very low  
327 (nearly the same level as that before the space weather event hit Mars) during some periods  
328 where blackouts were observed, like for example on the 18-20 September period. Moreover, it  
329 was demonstrated with the ionospheric simulation (see Figure 5) in which a precipitation  
330 electron flux with the same characteristics as during this event was included. Of course an

331 enhanced SEP proton flux could have contributed to even larger ionization levels, should their  
332 flux be high enough. Moreover, the radar attenuation could have been increased by the fact that  
333 the nightside electron precipitation was larger over crustal magnetic field regions. However, we  
334 note that SHARAD also suffered blackouts while sampling the northern hemisphere (far from  
335 crustal fields, see Figure 1 and SI), and MARSIS while sampling non-magnetized areas (such as  
336 longitudes  $\sim 0\text{-}90^\circ$ , see Figure 1 and SI).

337 Another question to discuss is the fact that energetic particles from the solar wind end up  
338 impacting on the nightside atmosphere of Mars. The MAVEN mission has revealed that diffuse  
339 aurora can be found at any location on the Martian nightside and is caused by SEPs, specifically  
340 electrons accelerated to energies of  $\sim 100$  keV at the Sun and heliospheric shock fronts (Schneider  
341 et al., 2015). For the time period of this study in September 2017, a 25 times brighter diffuse  
342 aurora was observed and detectable over the entire visible nightside. Schneider et al. (2018)  
343 showed that this aurora emission was originated from an altitude of  $\sim 60$  km in the atmosphere,  
344 which agrees well with the altitude in which the radio signals of both MARSIS and SHARAD radars  
345 were lost.

346 As shown in Figure 2, MARSIS operated in the active ionospheric mode during one orbit when the  
347 ICME was transiting Mars. Harada et al. (2018) reported that during this event the nightside peak  
348 electron density increased to unusually high values of  $\sim 1\text{-}2 \times 10^{10} \text{ m}^{-3}$  at around 120 km. The  
349 magnitude of this reported layer is of the same order as our model results in Figure 5c. However,  
350 the reported altitude of the maximum peak is  $\sim 30$  km higher than our simulations. A possible  
351 reason for this altitude discrepancy is that the electron flux in the simulation includes  
352 suprathermal electrons that are produced by high energy precipitating electrons above 20 keV.  
353 Since lower energy precipitating electrons are not considered, we lack secondary electrons of  
354 energy typically in the energy range 100-1000 eV which would produce ions at altitudes higher  
355 than 100 km (see Figure 5). Therefore, our simulation should be considered as a low limit  
356 estimation for altitudes larger than 100 km, where more ionization could have occurred.  
357 Nevertheless, higher-altitude ionization do not significantly change the radio absorption profile,  
358 which is the main focus of this paper. Another possible reason could be due to the process of  
359 deriving altitudes from MARSIS-AIS data, which is not straightforward (e.g. Morgan et al., 2013;  
360 Sanchez-Cano et al., 2012; 2013). In particular, the local plasma density measured at the  
361 spacecraft is needed for the computation of the altitude profile on the nightside, which is usually  
362 difficult to assess, giving uncertainties of tens of km (Andrews et al., 2013; Morgan et al., 2013).  
363 This question will be addressed in a future study.

364 Finally, attenuation estimates from this study agree well with previous theoretical (Witasse et al.,  
365 2001; Withers, 2011) and empirical studies (Nielsen et al., 2007; Morgan et al., 2006; Espley et  
366 al., 2007), although we note that all of them were related to dayside or post-terminator regions  
367 rather than the deep-nightside where our observations come from.

368

## 369 **7. Conclusions**

370 We have reported a long HF radar blackout, as shown in the data of the two current radars  
371 operating at Mars, MARSIS and SHARAD, during the strong space weather event in September  
372 2017 (Lee et al. 2018). Our interpretation is that the loss of signal is due to the formation of a  
373 lower ionospheric layer that absorbed HF radar waves, similar to PCA or *D*-layer absorption  
374 processes on Earth. Modelling shows that this ionospheric layer, created by SEP electrons, rather  
375 than previously proposed SEP protons, has a density of  $\sim 10^{10} \text{ m}^{-3}$  peaking at 90 km, and is mainly  
376 composed of  $\text{O}_2^+$  with a lesser contribution of  $\text{NO}^+$ .

377 This work allows us to identify the need for careful assessments of radar performances for future  
378 operational systems. Since these low ionospheric layers produce radar signal losses at least  
379 between 3 and 20 MHz, the outcome of this work allows a better assessment of high frequency  
380 radar performances during future space weather events. In those cases, a good characterization  
381 of the low ionosphere is necessary for radar operations (and other instruments that use HF radio  
382 links), operational planning, as well as for communications with the Martian surface in the HF  
383 range. This case also gives the possibility for the radar teams to flag the quality of data for the  
384 legacy archive.

385

## 386 **Acknowledgements**

387 B.S.-C., M.L. and S.E.M. acknowledge support through STFC grant ST/N000749/1. ESA-ESTEC  
388 Faculty is gratefully acknowledged. F.L. was supported by CNES "Système Solaire" program and  
389 by the Programme National de Planétologie and by the ANR (ANR-09-BLAN-0223) and ANR  
390 MARMITE (ANR-13-BS05-0012-02). IPIM model simulations can be freely requested at IRAP-  
391 CDPP web (<http://transplanet.irap.omp.eu/>). IPIM model is a property of CNRS. Part of this work  
392 and IPIM are supported by the Programme National Soleil Terre (PNST) from Institut des  
393 Sciences de l'Univers of Centre National de la Recherche Scientifique (INSU/CNRS) co-funded by  
394 CNES. This work was granted access to the HPC resources of CALMIP supercomputing center  
395 under the allocation 2017-P1520. Authors thank Matteo Crismani, Wlodek Kofman and Cyril

396 Grima for useful discussions. MEX data can be downloaded from the ESA-PSA archive, and MRO  
397 and MAVEN data from the NASA-PDS archive.

398

399

#### 400 **References**

401 – Andrews, D. J., H. J. Opgenoorth, N. J. T. Edberg, M. Andre, M. Franz, E. Dubinin, F. Duru, D.  
402 Morgan, and O. Witasse (2013), Determination of local plasma densities with the MARSIS  
403 radar: Asymmetries in the high-altitude Martian ionosphere, *J. Geophys. Res. Space*  
404 *Physics*, **118**, 6228–6242, doi:[10.1002/jgra.50593](https://doi.org/10.1002/jgra.50593).

405

406 – Andrews, D. J., et al. (2016), Plasma observations during the Mars atmospheric “plume” event  
407 of March–April 2012, *J. Geophys. Res. Space Physics*, **121**, doi:[10.1002/2015JA022023](https://doi.org/10.1002/2015JA022023).

408

409 – Blelly, P.-L., Lilensten, J., Robineau, A., Fontanari, J., & Alcayde, D. (1996). Calibration of a  
410 numerical ionospheric model with EISCAT observations. *Annales de Geophysique*, **14**(12),  
411 1375–1390. <https://doi.org/10.1007/s005850050399>

412

413 – Blelly, P. L., Lathuillere, C., Emery, B., Lilensten, J., Fontanari, J., & Alcayde, D. (2005). An  
414 extended TRANSCAR model including ionospheric convection: Simulation of EISCAT  
415 observations using inputs from AMIE. *Annales de Geophysique*, **23**(2), 419–  
416 431. <https://doi.org/10.5194/angeo-23-419-2005>

417

418 – Blelly, P.-L., A. Marchaudon, M. Indurain, O. Witasse, J. Amaya, B. Chide, N. André, V. Génot, A.  
419 Goutenoir, M. Bouchemit, (2019), Transplanet: A web service dedicated to modeling of  
420 planetary ionospheres, *Planetary and Space Science*, ISSN 0032-0633,  
421 <https://doi.org/10.1016/j.pss.2019.02.008>.

422

423 – Bones, D., J. M. C. Plane, and W. Feng (2015): Dissociative Recombination of FeO<sup>+</sup> with  
424 Electrons: Implications for Plasma Layers in the Ionosphere, *J. Phys. Chem. A*, **120**, 1369-1376.

425

426 – Campbell, B. A., N. E. Putzig, F. J. Foss, and R. J. Phillips, (2014), SHARAD signal attenuation and  
427 delay offsets due to the Martian ionosphere, *IEEE Geosci. Remote Sens. Lett.*, **11**(3),  
428 doi:[10.1109/LGRS.2013.2273396](https://doi.org/10.1109/LGRS.2013.2273396).

429

- 430 – Cartacci, M., Amata, E., Cicchetti, A., Noschese, R., Giuppi, S., Langlais, B., et al. (2013). Mars  
431 ionosphere total electron content analysis from MARSIS subsurface data. *Icarus*, **223**(1), 423–  
432 437. <https://doi.org/10.1016/j.icarus.2012.12.011>  
433
- 434 – Cartacci, M., Sánchez-Cano, B., Orosei, R., Noschese, R., Cicchetti, A., Witasse, O., et al.  
435 (2018). Improved estimation of Mars ionosphere total electron content. *Icarus*, **299**, 396–  
436 410. <https://doi.org/10.1016/j.icarus.2017>  
437
- 438 – Chicarro, A., P. Martin, and R. Traunter (2004), Mars Express: A European Mission to the Red  
439 Planet SP-1240, pp. 3–16, Eur. Space Agency Publ. Div., Noordwijk, Netherlands.  
440
- 441 – Crismani, M. M., Schneider, N. M., Plane, J. M., Evans, J. S., Jain, S. K., Chaffin, M. S., ... Jakosky, B.  
442 M. (2017). Detection of a persistent meteoric metal layer in the Martian atmosphere. *Nature*  
443 *Geoscience*, 10(6), 401–404.  
444
- 445 – Edberg, N. J. T., M. Lester, S. W. H. Cowley, and A. I. Eriksson (2008), Statistical analysis of the  
446 location of the Martian magnetic pileup boundary and bow shock and the influence of crustal  
447 magnetic fields, *J. Geophys. Res.*, 113, A08206, doi:10.1029/2008JA013096.  
448
- 449 – Eparvier, F. G., Chamberlin, P. C., Woods, T. N., & Thiemann, E. M. B. (2015). The solar extreme  
450 ultraviolet monitor for MAVEN. *Space Science Reviews*, **195**(1-4), 293–  
451 301. <https://doi.org/10.1007/s11214-015-0195-2>  
452
- 453 – Espley, J. R., W. M. Farrell, D. A. Brain, D. D. Morgan, B. Cantor, J. J. Plaut, M. H. Acuña, and G.  
454 Picardi (2007), Absorption of MARSIS radar signals: Solar energetic particles and the daytime  
455 ionosphere, *Geophys. Res. Lett.*, 34, L09101, doi:10.1029/2006GL028829.  
456
- 457 – Fillingim, M. O., L. M. Peticolas, R. J. Lillis, D. A. Brain, J. S. Halekas, D. L. Mitchell, R. P. Lin,  
458 D. Lummerzheim, S. W. Bougher, and D. L. Kirchner (2007), Model calculations of electron  
459 precipitation induced ionization patches on the nightside of Mars, *Geophys. Res. Lett.*, 34,  
460 L12101, doi:10.1029/2007GL029986  
461
- 462 – Forget, F., Hourdin, F., Fournier, R., Hourdin, C., Talagrand, O., Collins, M., et al.  
463 (1999). Improved general circulation models of the Martian atmosphere from the surface to  
464 above 80 km. *Journal of Geophysical Research*, **104**, 24,155–24,175.  
465

- 466 – Fox, J. L., Brannon, J. F., & Porter, H. S. (1993). Upper limits to the nightside ionosphere of Mars.  
467 *Geophysical Research Letters*, 20, 1339–1342. <https://doi.org/10.1029/93GL01349>  
468
- 469 – Girazian, Z., P. R. Mahaffy, R. J. Lillis, M. Benna, M. Elrod, and B. M. Jakosky (2017a), Nightside  
470 ionosphere of Mars: Composition, vertical structure, and variability, *J. Geophys. Res. Space*  
471 *Physics*, 122, 4712–4725, doi: 10.1002/2016JA023508.  
472
- 473 – Girazian, Z., Mahaffy, P., Lillis, R. J., Benna, M., Elrod, M., Fowler, C. M., & Mitchell, D. L. (2017b).  
474 Ion densities in the nightside ionosphere of Mars: Effects of electron impact ionization.  
475 *Geophysical Research Letters*, 44, 11,248–11,256. <https://doi.org/10.1002/2017GL075431>  
476
- 477 – Guo, J., Dumbovic, M., Wimmer-Schweingruber, R., F., Temmer, M., Lohf, H., Wang, Y., Veronig,  
478 A., Hassler, D. M., Mays, L. M., Zeitlin, C., Ehresmann, B., Witasse, O., von Forstner, J. L., F., Heber,  
479 B., Holmstrom, M., Posner, A.: 2018, Modeling the evolution and propagation of the 2017  
480 September 9th and 10th CMEs and SEPs arriving at Mars constrained by remote-sensing and  
481 in-situ measurement, *Space Weather*, 16, 1156–1169,  
482 <https://doi.org/10.1029/2018SW001973>  
483
- 484 – Hall, B. E. S., et al. (2016), Annual variations in the Martian bow shock location as observed by  
485 the Mars express mission, *J. Geophys. Res. Space Physics*, 121, 11,474–11,494,  
486 doi:10.1002/2016JA023316.  
487
- 488 – Harada, Y., Gurnett, D. A., Kopf, A. J., et al.: 2018, MARSIS observations of the Martian nightside  
489 ionosphere during the September 2017 solar event, *Geophys. Res. Lett.*, 45, 7960–  
490 7967, doi:10.1002/2018GL077622.  
491
- 492 – Itikawa, Y., Momentum transfer cross sections for electron collisions with atoms and  
493 molecules, *At. Data Nucl. Data Tables*, 21, 69, 1978.  
494
- 495 – Jiggins et al., (2018), In-Situ Data and Effect Correlation During September 2017 Solar Particle  
496 Event. *Space Weather*, 16. <https://doi.org/10.1029/2018SW001936>  
497
- 498 – Larson, D., Lillis, R. J., Lee, C. O., Dunn, P. A., Hatch, K., Robinson, M., et al. (2015). The MAVEN  
499 solar energetic particle investigation. *Space Science Reviews*, 175, 153–  
500 172. <https://doi.org/10.1007/s11214-015-0218-z>  
501

- 502 – Leblanc, F., O. Witasse, J. Winningham, D. Brain, J. Lilensten, P.-L. Blelly, R. A. Frahm, J. S.  
503 Halekas, and J. L. Bertaux (2006), Origins of the Martian aurora observed by Spectroscopy for  
504 Investigation of Characteristics of the Atmosphere of Mars (SPICAM) on board Mars Express,  
505 *J. Geophys. Res.*, 111, A09313, doi:10.1029/2006JA011763.
- 506
- 507 – Lee, C. O., Jakosky, B. M., Luhmann, J. G., Brain, D. A., Mays, M. L., Hassler, D. M., et al.  
508 (2018). Observations and impacts of the 10 September 2017 solar events at Mars: An overview  
509 and synthesis of the initial results. *Geophysical Research Letters*, 45, 8871–  
510 8885. <https://doi.org/10.1029/2018GL079162>
- 511
- 512 – Lillis, R. J., M. O. Fillingim, and D. A. Brain (2011), Three-dimensional structure of the Martian  
513 nightside ionosphere: Predicted rates of impact ionization from Mars Global Surveyor  
514 MAG/ER measurements of precipitating electrons, *J. Geophys. Res.*, 116, A12317,  
515 doi:10.1029/2011JA016982.
- 516
- 517 – Lillis, R. J., & Fang, X. (2015). Electron impact ionization in the Martian atmosphere: Interplay  
518 between scattering and crustal magnetic field effects. *Journal of Geophysical Research:*  
519 *Planets*, 120, 1332–1345. <https://doi.org/10.1002/2015JE004841>
- 520
- 521 – Lillis, R. J., Mitchell, D. L., Steckiewicz, M., Brain, D., Xu, S., Weber, T., et al. (2018). Ionizing  
522 electrons on the Martian nightside: Structure and variability. *Journal of Geophysical Research:*  
523 *Space Physics*, 123, 4349–4363. <https://doi.org/10.1029/2017JA025151>
- 524
- 525 – Marchaudon, A., P.-L. Blelly, (2015), A new 16-moment interhemispheric model of the  
526 ionosphere: IPIM, *J. Geophys. Res.*, 120, doi: 10.1002/2015JA021193
- 527
- 528 – Millour, E., Forget, F., Spiga, A., Navarro, T., Madeleine, J.-B., Montabone, L., et al. (2015). The  
529 Mars Climate Database (MCD version 5.2), in European Planetary Science Congress 2015, vol.  
530 10, EPSC2015–438, Nantes, France, 27 Sept.–2 Oct.
- 531
- 532 – Molina-Cuberos, G. J., O. Witasse, J.-P. Lebreton, R. Rodrigo, and J. J. Lopez-Moreno (2003),  
533 Meteoric ions in the atmosphere of Mars, *Planet. Space Sci.*, 51, 239– 249.
- 534
- 535 – Morel, L., Witasse, O., Warnant, R., Cerisier, J.-C., Blelly, P.-L., & Lilensten, J. (2004). Diagnostic  
536 of the dayside ionosphere of Mars using the total electron content measurement by the  
537 NEIGE/Netlander experiment: An assessment study. *Planetary and Space Science*, 52(7), 603–  
538 611. <https://doi.org/10.1016/j.pss.2003.12.007>

539

540 – Morgan, D. D., D. A. Gurnett, D. L. Kirchner, R. L. Huff, D. A. Brain, W. V. Boyton, M. H. Acuña, J. J.  
541 Plaut, and G. Picardi (2006), Solar control of radar wave absorption by the Martian ionosphere,  
542 *Geophys. Res. Lett.*, **33**, L13202, doi:10.1029/2006GL026637.

543

544 – Morgan, D. D., et al. (2010), Radar absorption due to a corotating interaction region encounter,  
545 *Icarus*, **206**, 95–103. <https://doi.org/10.1016/j.icarus.2009.03.008>

546

547 – Morgan, D. D., O. Witasse, E. Nielsen, D. A. Gurnett, F. Duru, and D. L. Kirchner (2013), The  
548 processing of electron density profiles from the Mars Express MARSIS topside sounder, *Radio*  
549 *Sci.*, **48**, 197–207, doi:10.1002/rds.20023.

550

551 – Morgan, D. D., Diéval, C., Gurnett, D. A., Duru, F., Dubinin, E. M., Fränz, M., et al. (2014). Effects  
552 of a strong ICME on the Martian ionosphere as detected by Mars Express and Mars  
553 Odyssey. *Journal of Geophysical Research: Space Physics*, **119**, 5891–  
554 5908. <https://doi.org/10.1002/2013JA019522>

555

556 – Mouginot, J., Kofman, W., Safaeinili, A., & Herique, A. (2008). Correction of the ionospheric  
557 distortion on the MARSIS surface sounding echoes. *Planetary and Space Science*, **56**(7), 917–  
558 926. <https://doi.org/10.1016/j.pss.2008.01.010>

559

560 – Němec, F., D. D. Morgan, C. Dieval, D. A. Gurnett, and Y. Futaana (2014), Enhanced ionization of  
561 the Martian nightside ionosphere during solar energetic particle events, *Geophys. Res. Lett.*, **41**,  
562 793–798, doi:10.1002/2013GL058895.

563

564 – Němec, F., D. D. Morgan, C. Dieval, and D. A. Gurnett (2015), Intensity of nightside MARSIS AIS  
565 surface reflections and implications for low-altitude ionospheric densities, *J. Geophys. Res.*  
566 *Space Physics*, **120**, doi:10.1002/2014JA020888.

567

568 – Nielsen, E., D. D. Morgan, D. L. Kirchner, J. J. Plaut, and G. Picardi (2007), Absorption and  
569 reflection of radio waves in the Martian ionosphere, *Planet. Space Sci.*, **55**, 864–870,  
570 doi:10.1016/j.pss.2006.10.005.

571

572 – Orosei, R., Jordan, R. L., Morgan, D. D., Cartacci, M., Cicchetti, A., Duru, F., et al. (2015). Mars  
573 Advanced Radar for Subsurface and Ionospheric Sounding (MARSIS) after nine years of  
574 operation: A summary. *Planetary and Space Science*, **112**, 98–  
575 114. <https://doi.org/10.1016/j.pss.2014.07.010>

- 576  
577 – Pesnell, W. D., and Grebowsky, J., Meteoric magnesium ions in the Martian atmosphere, J.  
578 Geophys. Res., 105, 1695, 2000.
- 579  
580 – Picardi, G., Biccari, D., Seu, R., Plaut, J., Johnson, W. T. K., Jordan, R. L., et al. (2004). MARSIS:  
581 Mars advanced radar for subsurface and ionosphere sounding. In A. Wilson & A. Chicarro  
582 (Eds.), *Mars Express: The scientific payload* (Vol. **1240**, pp. 51–69). Noordwijk, Netherlands:  
583 ESA Special Publication.
- 584  
585 – Plane, J.M.C. (2003), Atmospheric Chemistry of Meteoric Metals, *Chemical Reviews*, 103, 4963-  
586 4984
- 587  
588 – Plane, J. M. C.; J. D. Carrillo-Sanchez, T. P. Mangan, M. M. J. Crismani, N. M. Schneider, and A.  
589 Määttänen (2018), Meteoric Metal Chemistry in the Martian Atmosphere, *J. Geophys. Res. –*  
590 *Planets*, 123, 695-707, doi:10.1002/2017JE005510.
- 591  
592 – Ramírez-Nicolás, B., Sánchez-Cano, O., Witasse, P.-L., Brelly, L., & Vázquez, M. L. (2016). The  
593 effect of the induced magnetic field on the electron density vertical profile of the Mars'  
594 ionosphere: A Mars Express MARSIS radar data analysis and interpretation, a case  
595 study. *Planetary and Space Science*, **126**, 49–62. <https://doi.org/10.1016/j.pss.2016.03.017>
- 596  
597 – Redmon, R. J., Seaton, D. B., Steenburgh, R., He, J., & Rodriguez, J. V. (2018). September 2017's  
598 geoeffective space weather and impacts to Caribbean radio communications during hurricane  
599 response. *Space Weather*, 16, 1190–1201. <https://doi.org/10.1029/2018SW001897>
- 600  
601 – Rees, M. (1989). The interaction of energetic electrons and ions with the upper atmosphere.  
602 In *Physics and Chemistry of the Upper Atmosphere* (Cambridge Atmospheric and Space  
603 Science Series, Chapter 3). Cambridge: Cambridge University Press.  
604 doi:10.1017/CBO9780511573118.004
- 605  
606 – Safaeinili, A., W. Kofman, J. Nouvel, A. Herique, and R. L. Jordan (2003), Impact of Mars  
607 ionosphere on orbital radar sounder operation and data processing, *Planet. Space Sci.*, 51,  
608 505–515.
- 609  
610 – Safaeinili, A., Kofman, W., Mouginot, J., Gim, Y., Herique, A., Ivanov, A. B., et al.  
611 (2007). Estimation of the total electron content of the Martian ionosphere using radar sounder

- 612 surface echoes. *Geophysical Research Letters*, 34, L23204.  
613 <https://doi.org/10.1029/2007GL032154>
- 614
- 615 – Sánchez-Cano, B., O. Witasse, M. Herraiz, S. M. Radicella, J. Bauer, P.-L. Blelly, and G. Rodríguez-  
616 Caderot (2012), Retrieval of ionospheric profiles from the Mars Express MARSIS experiment  
617 data and comparison with radio-occultation data, *Geosci. Instrum. Method Data Syst.*, **1**, 77–84,  
618 doi:[10.5194/gi-1-77-2012](https://doi.org/10.5194/gi-1-77-2012).
- 619
- 620 – Sánchez-Cano, B., S. M. Radicella, M. Herraiz, O. Witasse, and G. Rodríguez-Caderot  
621 (2013), NeMars: An empirical model of the Martian dayside ionosphere based on Mars Express  
622 MARSIS data, *Icarus*, **225**, 236–247, doi:[10.1016/j.icarus.2013.03.021](https://doi.org/10.1016/j.icarus.2013.03.021).
- 623
- 624 – Sánchez-Cano, B., Morgan, D. D., Witasse, O., Radicella, S. M., Herraiz, M., Orosei, R., et al.  
625 (2015a). Total electron content in the Martian atmosphere: A critical assessment of the Mars  
626 Express MARSIS data sets. *Journal of Geophysical Research: Space Physics*, **120**, 2166–  
627 2182. <https://doi.org/10.1002/2014JA020630>
- 628
- 629 – Sánchez-Cano, B., M. Lester, O. Witasse, S. E. Milan, B. E. S. Hall, P.-L. Blelly, S. M. Radicella, and  
630 D. D. Morgan (2015b), Evidence of scale height variations in the Martian ionosphere over the  
631 solar cycle, *J. Geophys. Res. Space Physics*, 120, doi:[10.1002/2015JA021949](https://doi.org/10.1002/2015JA021949).
- 632
- 633 – Sánchez-Cano, B., Lester, M., Witasse, O., Blelly, P.-L., Indurain, M., Cartacci, M., et al.  
634 (2018). Spatial, seasonal, and solar cycle variations of the Martian total electron content (TEC):  
635 Is the TEC a good tracer for atmospheric cycles? *Journal of Geophysical Research: Planets*, 123,  
636 1746–1759. <https://doi.org/10.1029/2018JE005626>
- 637
- 638 – Sánchez-Cano, B., et al. (2016), Solar cycle variations in the ionosphere of Mars as seen by  
639 multiple Mars Express data sets, *J. Geophys. Res. Space Physics*, 121,  
640 doi:[10.1002/2015JA022281](https://doi.org/10.1002/2015JA022281).
- 641
- 642 – Schneider, N. M., Deighan, J. I., Jain, S. K., Stiepen, A., Stewart, A. I. F., Larson, D., et al. (2015).  
643 Discovery of diffuse aurora on Mars. *Science*, 350(6261), aad0313.  
644 <https://doi.org/10.1126/science.aad0313>
- 645
- 646 – Schneider, N. M., Jain, S. K., Deighan, J., Nasr, C. R., Brain, D. A., Larson, D., et al. (2018). Global  
647 aurora on Mars during the September 2017 space weather event. *Geophysical Research*  
648 *Letters*, 45, 7391–7398. <https://doi.org/10.1029/2018GL077772>

649

650 – Schunk, R., and A. F. Nagy (2009), *Ionospheres: Physics, Plasma Physics, and Chemistry*,  
651 Cambridge Univ. Press, New York.

652

653 – Seu, R., D. Biccaldi, R. Orosei, L. V. Lorenzoni, R. J. Phillips, L. Marinangeli, G. Picardi, A. Masdea,  
654 and E. Zampolini (2004), SHARAD: The MRO 2005 shallow radar, *Planet. Space Sci.*, **52**, 157–  
655 166. <https://doi.org/10.1016/j.pss.2003.08.024>

656

657 – Sheel, V., S. A. Haider, P. Withers, K. Kozarev, I. Jun, S. Kang, G. Gronoff, and C. S. Wedlund  
658 (2012), Numerical simulation of the effects of a solar energetic particle event on the  
659 ionosphere of Mars, *J. Geophys. Res.*, **117**, A05312, doi:10.1029/2011JA017455.

660

661 – Ulusen, D., D. A. Brain, J. G. Luhmann, and D. L. Mitchell (2012), Investigation of Mars'  
662 ionospheric response to solar energetic particle events, *J. Geophys. Res.*, **117**, A12306,  
663 doi:10.1029/2012JA017671.

664

665 – Witasse, O. (2000), Modélisation des Ionosphères planétaires et de leur Rayonnement: La  
666 Terre et Mars, PhD thesis, Laboratoire de Planétologie de Grenoble.

667

668 – Witasse, O., J.-F. Nouvel, J.-P. Lebreton, and W. Kofman (2001), HF radio wave attenuation due  
669 to a meteoric layer in the atmosphere of Mars, *Geophys. Res. Lett.*, **28**, 3039– 3042.

670

671 – Witasse, O., Dutuit, O., Lilensten, J., Thissen, R., Zabka, J., Alcaraz, C., et al. (2002). Prediction of  
672 a CO<sub>2</sub><sup>2+</sup> layer in the atmosphere of Mars. *Geophysical Research Letters*, **29**(8),  
673 1263. <https://doi.org/10.1029/2002GL014781>

674

675 – Witasse, O., et al. (2003), Correction to “Prediction of a CO<sub>2</sub><sup>2+</sup> layer in the atmosphere of  
676 Mars”, *Geophys. Res. Lett.* **30**(7), 1360, doi:10.1029/2003GL017007.

677

678 – Withers, P. (2011), Attenuation of radio signals by the ionosphere of Mars: Theoretical  
679 development and application to MARSIS observations, *Radio Sci.*, **46**, RS2004,  
680 doi:10.1029/2010RS004450.

681

682 – Withers, P., M. O. Fillingim, R. J. Lillis, B. Häusler, D. P. Hinson, G. L. Tyler, M. Pätzold, K. Peter,  
683 S. Tellmann, and O. Witasse (2012), Observations of the nightside ionosphere of Mars by the  
684 Mars Express Radio Science Experiment (MaRS), *J. Geophys. Res.*, **117**, A12307,  
685 doi:10.1029/2012JA018185

686

687 – Zurek, R. W., and S. E. Smrekar (2007), An overview of the Mars Reconnaissance Orbiter  
688 (MRO) science mission, *J. Geophys. Res.*, 112, E05S01, doi: 10.1029/2006JE002701.

689

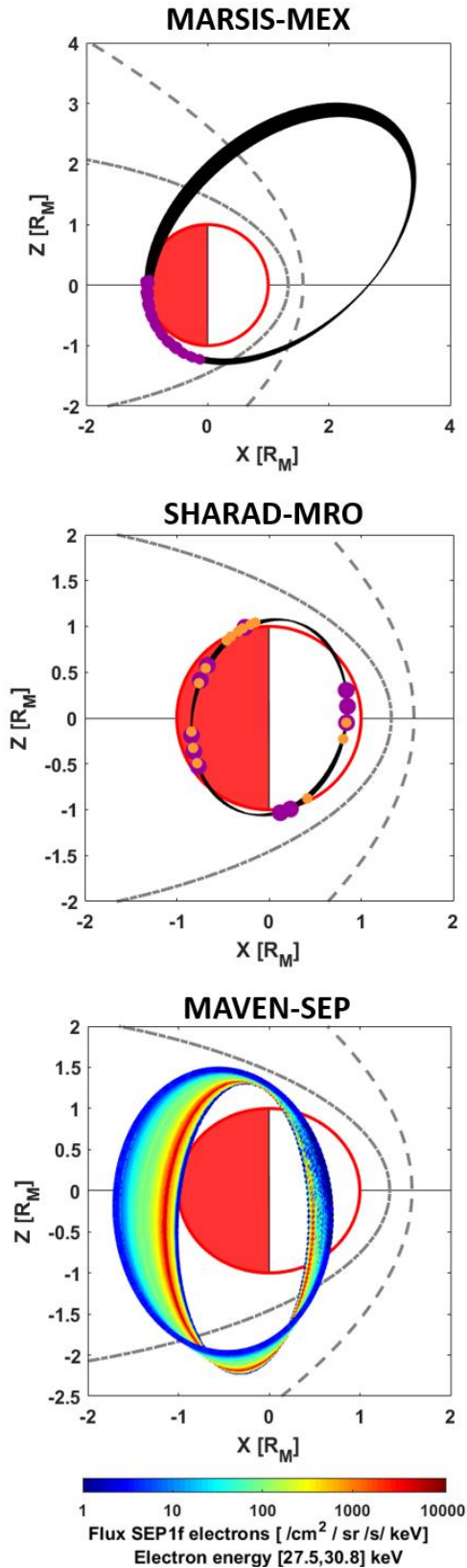
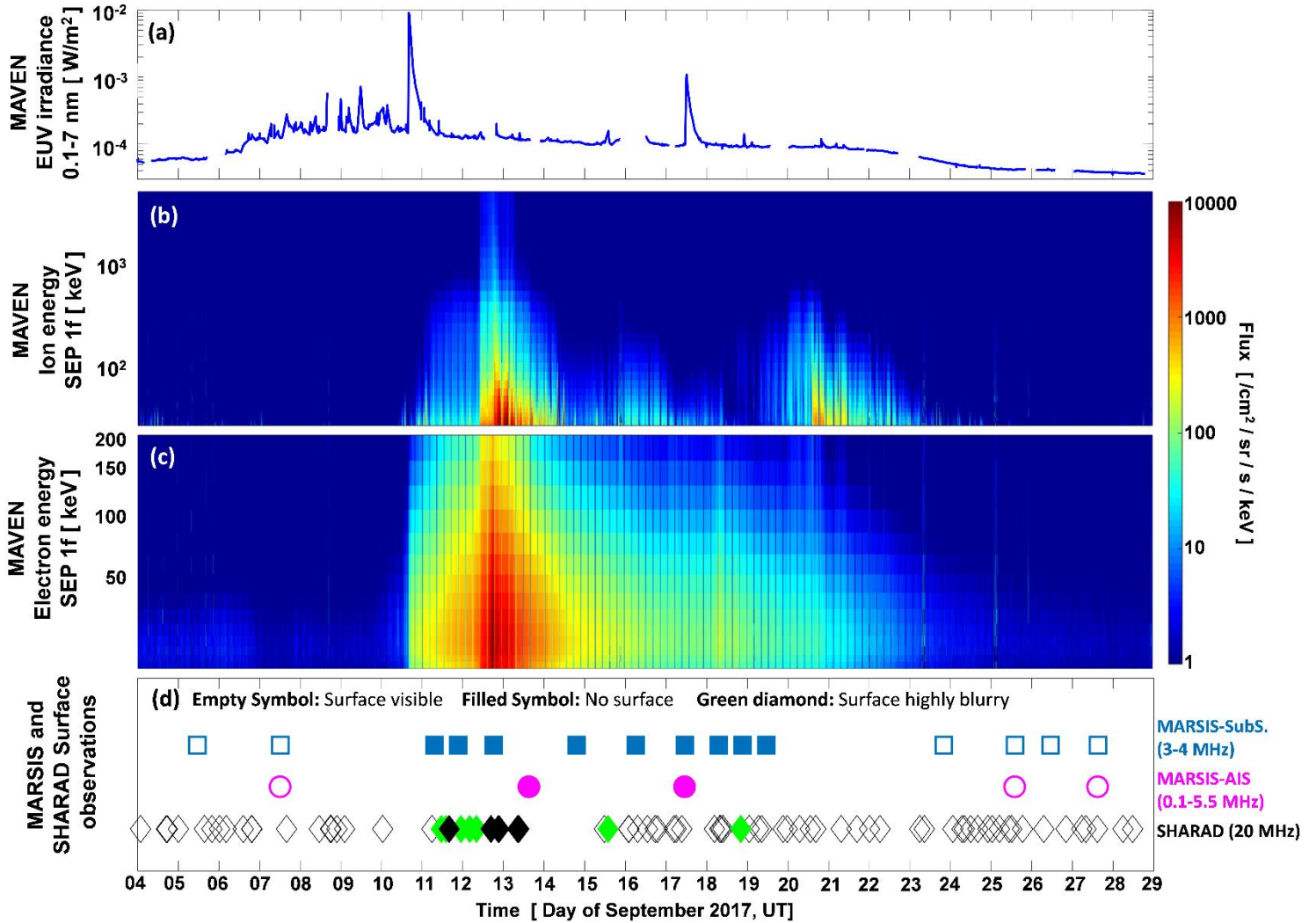
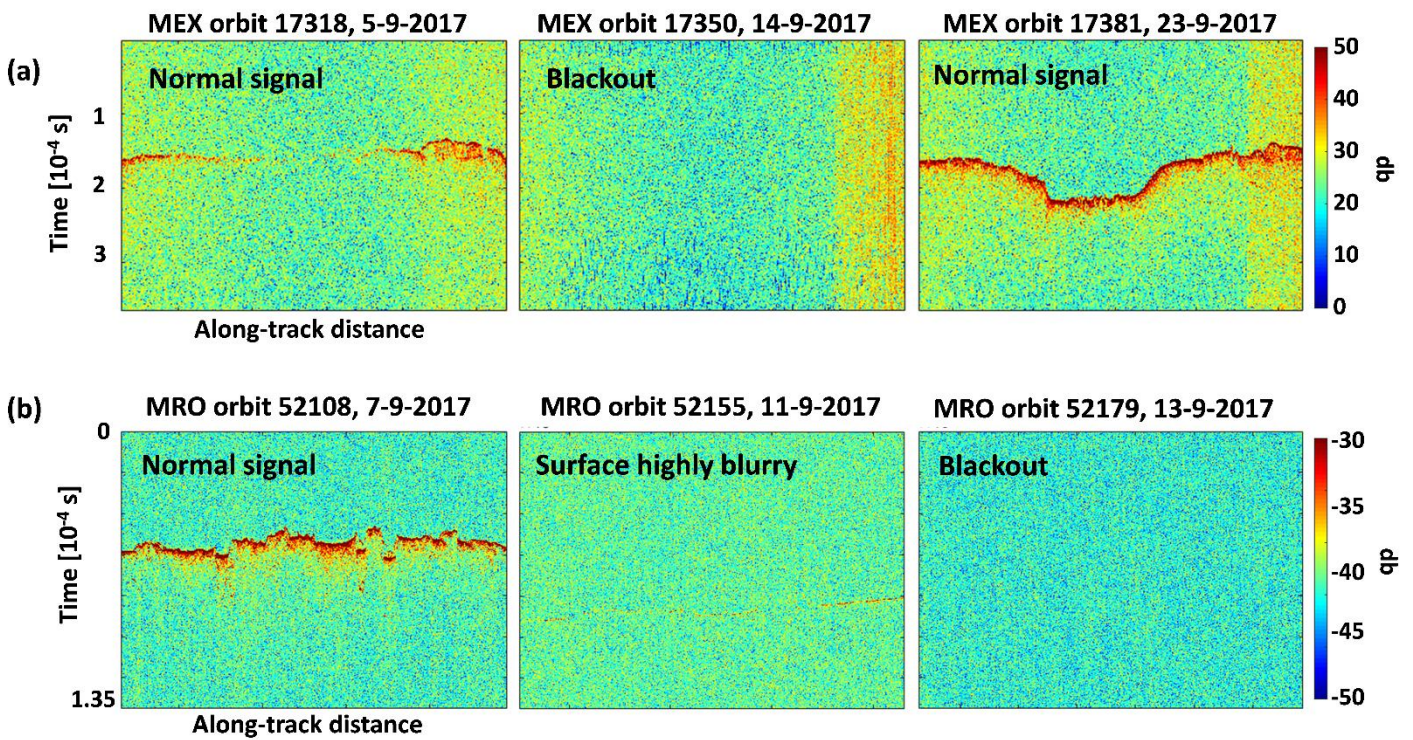


**Figure 1:** MEX, MRO and MAVEN orbits in the Z-X MSO plane. The rest of the orbital planes, as well as the latitude-longitude coordinates can be found in the SI material. The Sun is to the right. A grey dash-dotted line indicates the magnetic pileup boundary position (Edberg et al. 2008), and a grey dashed line the bow shock position (Hall et al., 2016). (Top panel) Blackout locations of MARSIS-MEX radar in purple circles. (Middle panel) Total blackout locations of SHARAD-MRO radar in purple circles, and partial blackouts (highly-blurry surface observations) in orange circles. (Bottom panel) MAVEN-SEP flux observations (color-coded) along its orbit. The electron flux used in this figure correspond to the energy interval 27.5-30.8 keV.

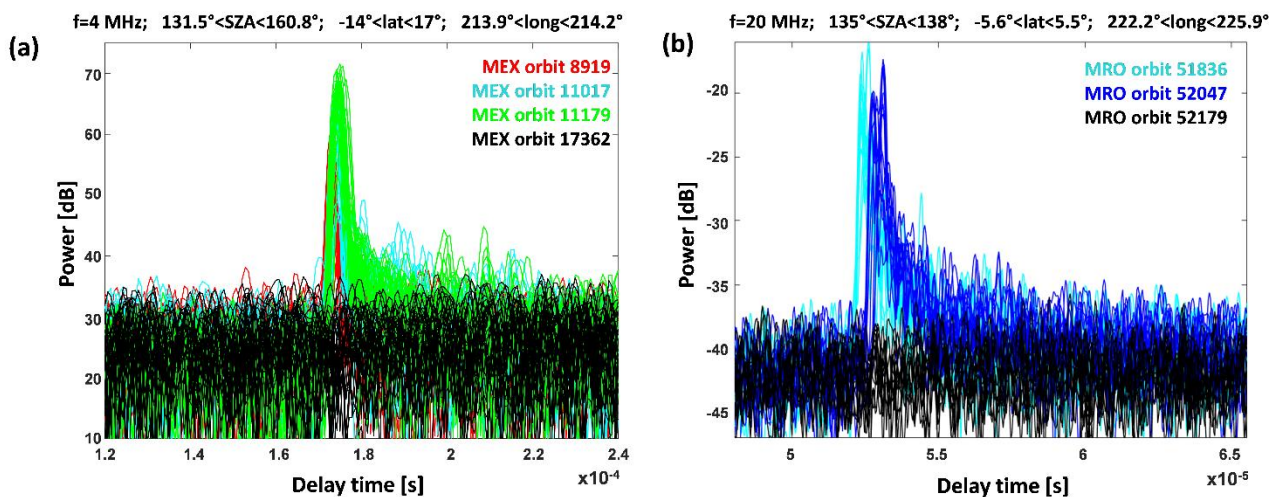


718 **Figure 2:** (a) MAVEN-EUV irradiance observations of wavelength 0.1-7 nm. (b) MAVEN-SEP ion  
 719 differential flux spectra. (c) MAVEN-SEP electron differential flux spectra. (d) Each symbol  
 720 denotes when MARSIS and SHARAD were in operation. Empty symbols designate the cases when  
 721 the surface was observed, and filled symbols when was not observed. The exception are green  
 722 diamonds that indicate the times when SHARAD observed a highly blurry surface.

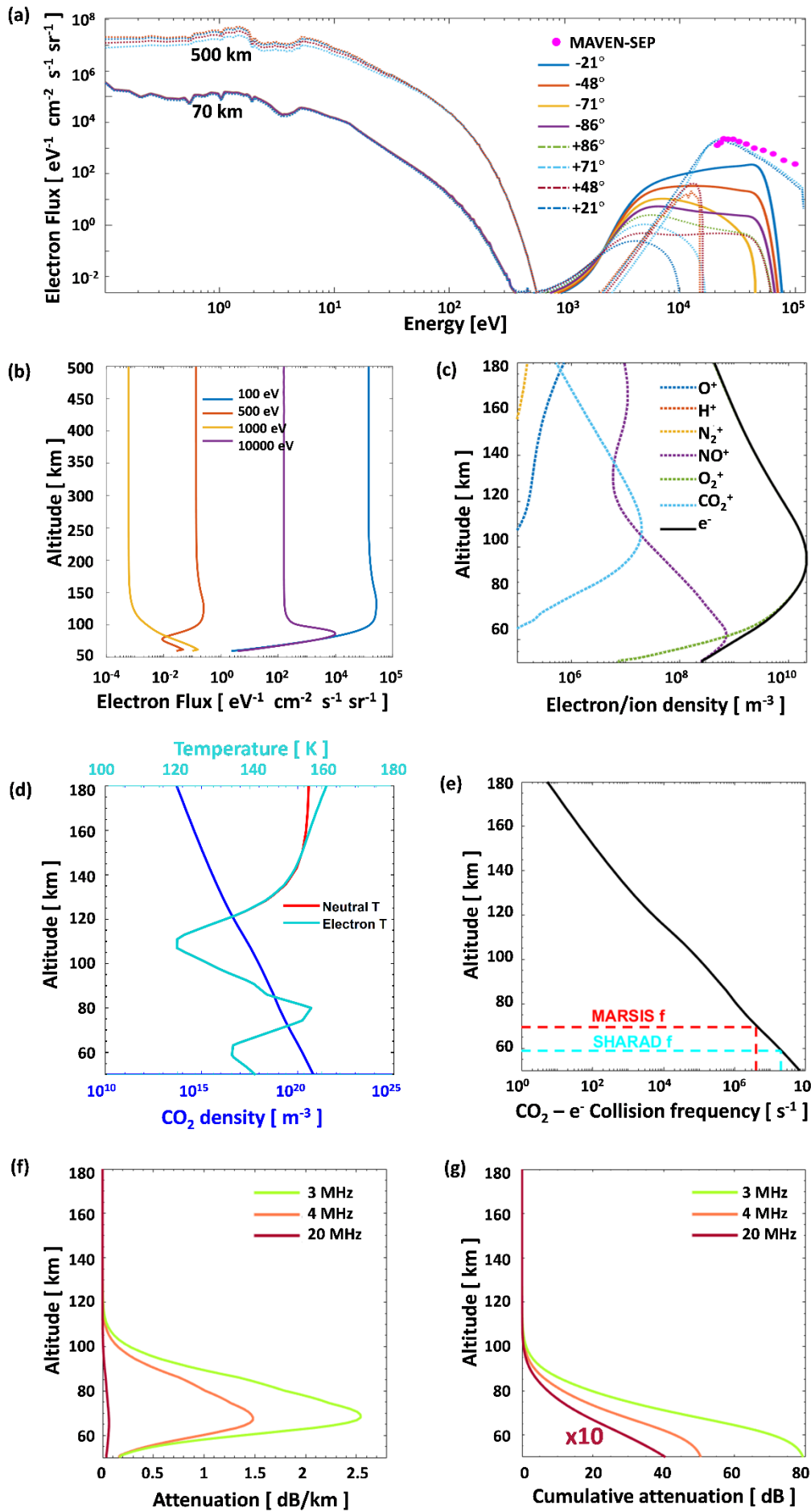


724 **Figure 3:** Radargram examples showing normal surface reflections, blackouts and partial  
 725 blackouts (surface highly blurry). (a) MARSIS radargrams. (b) SHARAD radargrams

726



7. **Figure 4:** (a) MARSIS power signal versus delay time for several orbits over the same region. (b)  
 728 SHARAD power signal versus delay time for several orbits over the same region.  
 729



731 **Figure 5:** IPIM simulation results. (a) Electron flux as a function of energy at 500 and 70 km. A  
732 positive angle means downward flux, and a negative, upward flux. (b) Electron flux profile as a  
733 function of altitude for four different energies. (c) Electron density and main ions altitude profiles.  
734 (d) Electron and neutral temperatures and CO<sub>2</sub> density profiles with altitude. (e) Electron-CO<sub>2</sub>  
735 collision frequency. The altitude at which the MARSIS and SHARAD frequencies equal the collision  
736 frequency are indicated with dashed-lines (f) Attenuation profiles with altitude for each radar  
737 frequency. (g) Same as (f) but shown as a cumulative integration. We note that the cumulative  
738 attenuation for 20 MHz has been multiplied by the factor 10 for better visualization.

739

740

741

742

743

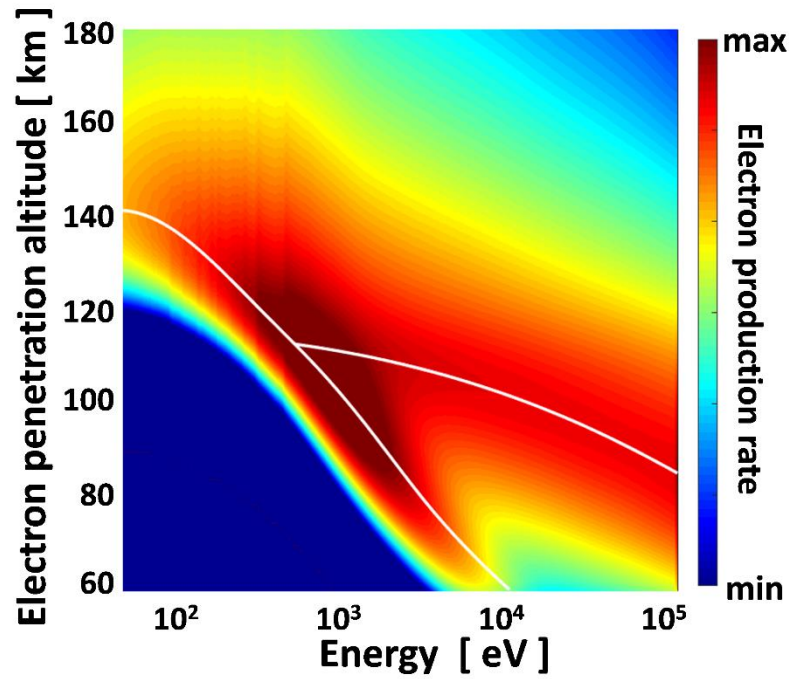
744

745

746

747

748



749

750 **Figure 6:** Electron penetration depth versus energy. The white line indicates the altitude where  
751 the precipitating electrons are stopped. The upper white line at energy > 500 eV is related to  
752 secondary electrons, while the lower one is related to the primary electrons.

753

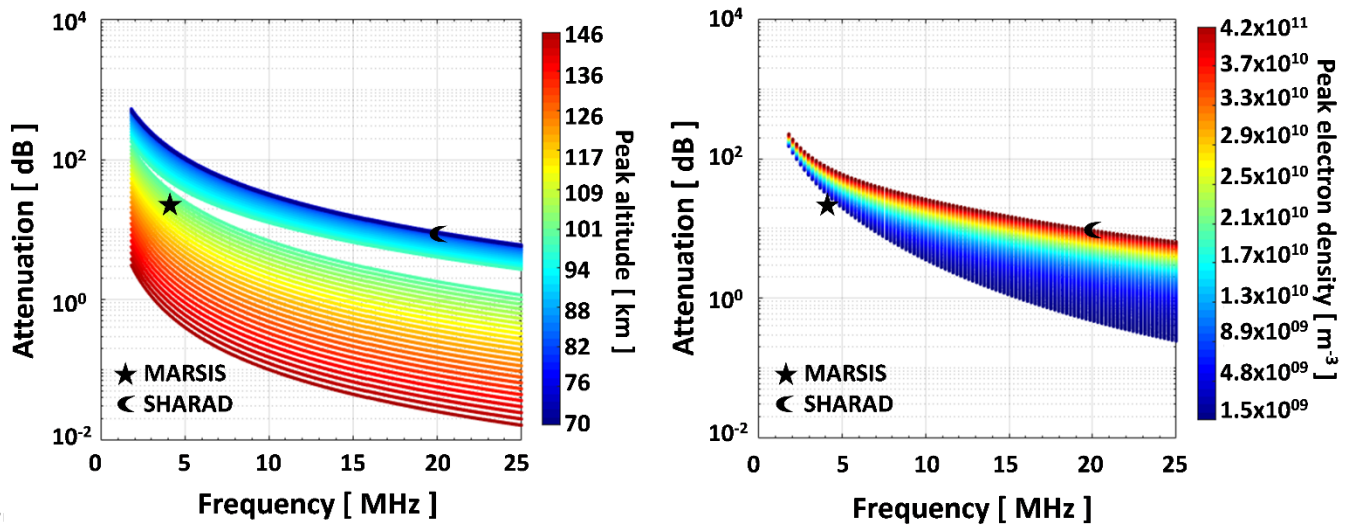
754

755

756

757

758



760 **Figure 7:** (Left panel) Total attenuation versus radar frequency for the electron density profile of  
 761 Figure 5c at different altitudes. (Right panel) Total attenuation versus radar frequency for  
 762 different electron density peak values of profile of Figure 5c. A star indicates the estimated lower  
 763 bound on MARSIS attenuation, the crescent marks the attenuation measured for SHARAD.

764  
 765  
 766  
 767  
 768